Supplementary Information

Multiscale integral synchronous assembly of cuttlebone-inspired structural materials by predesigned hydrogels

Huai-Bin Yang[1]†, Yi-Xing Lu[1]†, Xin Yue[1]†, Zhao-Xiang Liu[1], Wen-Bin Sun[1], Wen-Pei Zheng[1], Qing-Fang Guan[1]* & Shu-Hong Yu[1,2]*

[1] *Department of Chemistry, New Cornerstone Science Institute, Institute of Biomimetic Materials & Chemistry, Anhui Engineering Laboratory of Biomimetic Materials, Division of Nanomaterials & Chemistry, Hefei National Research Center for Physical Sciences at the Microscale, University of Science and Technology of China, Hefei 230026, China.*

[2] *Institute of Innovative Materials (I2M), Department of Materials Science and Engineering, Department of Chemistry, Southern University of Science and Technology, Shenzhen 518055, China.*

*Correspondence to: Qing-Fang Guan (guanqf@ustc.edu.cn); Shu-Hong Yu (shyu@ustc.edu.cn or yush@sustech.edu.cn).

† These authors contributed equally to this work.

This PDF file includes:

Supplementary Figures 1 to 28

Supplementary Tables 1 to 3

Supplementary References

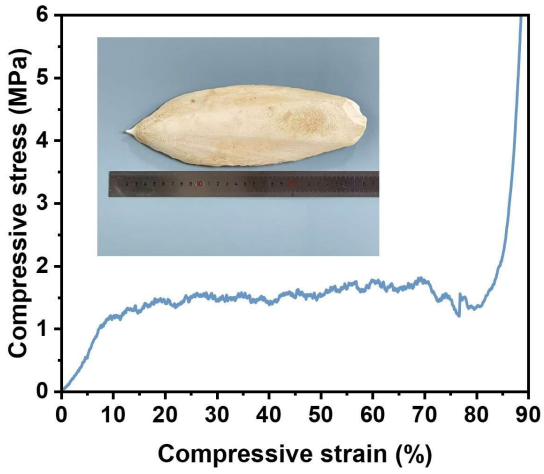

Supplementary Figure 1 | Compressive stress–strain curve of natural cuttlebone. The curve embodies the remarkable plateau stage, demonstrating the excellent energy absorption property of natural cuttlebone. Inset: photograph of a natural cuttlebone.

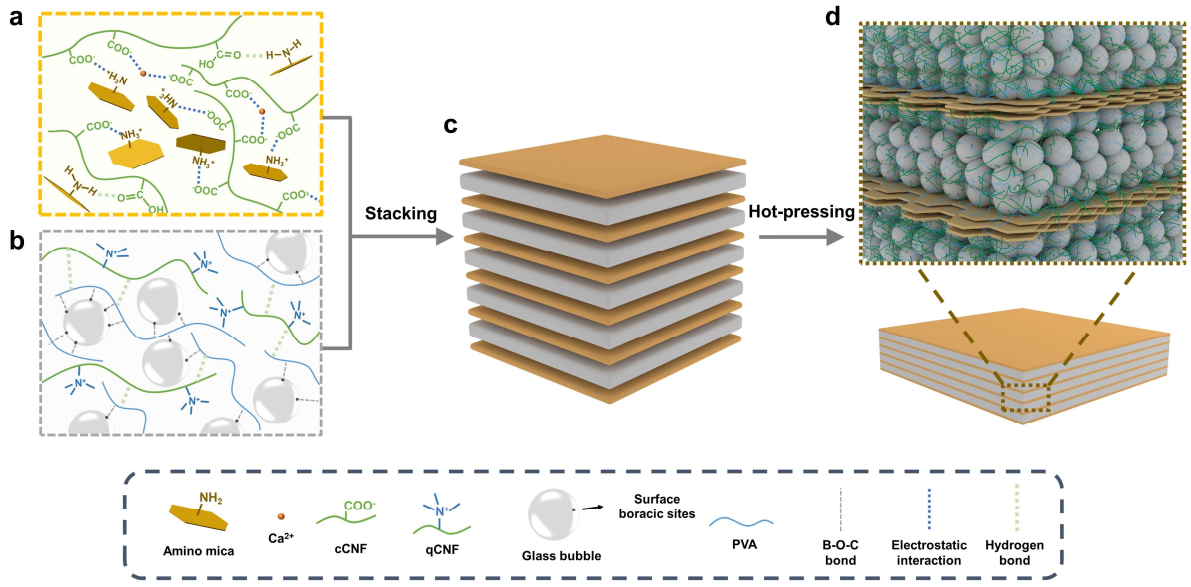

Supplementary Figure 2 | Fabrication process of rigid cavity-wall structural material (RCWSM). The various microstructures within the RCWSM were derived from the assembly system in the corresponding predesigned initial gel. **a**, In the initial gel of the wall structure, amino mica platelets were sufficiently assembled with cCNF through Ca^{2+} crosslinking and interactions between carboxyl groups and amino groups. **b**, In the initial gel of the rigid cavity layer, GB was tightly assembled with PVA and qCNF through notable B-O-C bonds and hydrogen bonds. **c**, For the fabrication of a cuttlebone-inspired sophisticated lamellar structure, each initial gel was evenly divided and layer-by-layer stacked in sequence. **d**, Finally, the RCWSM was obtained by hot-pressing. The brick-and-mortar structure wall layer and the close-packed rigid micro hollow structure were assembled during this process.

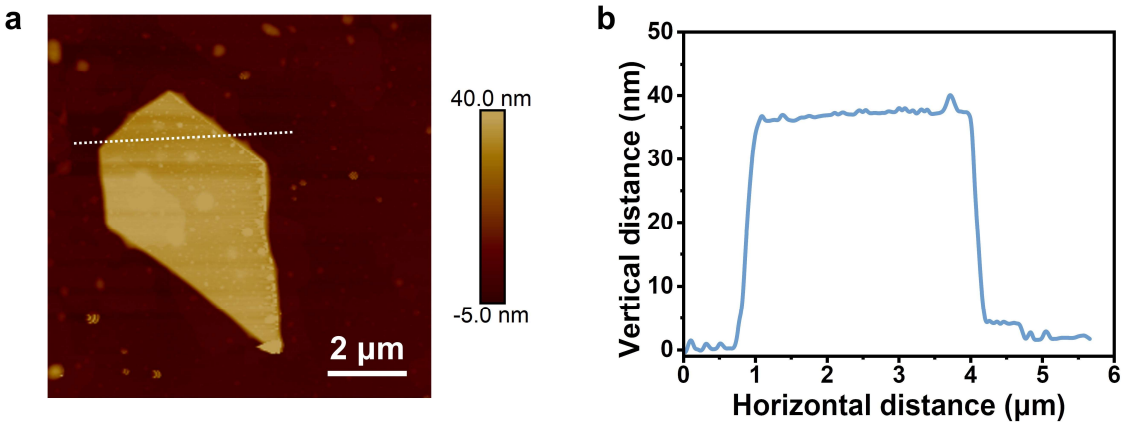

Supplementary Figure 3 | Morphological characterization of amino mica. a, AFM image of amino mica. **b**, The relative height corresponding to the line in Supplementary Figure 3a.

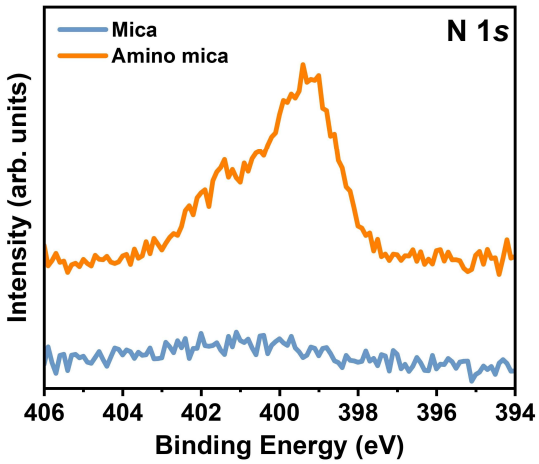

Supplementary Figure 4 | N 1*s* XPS spectra of mica and amino mica. The results illustrate the strong N element signal in mica after surface amination, demonstrating the presence of amino groups on the surface of the amino mica.

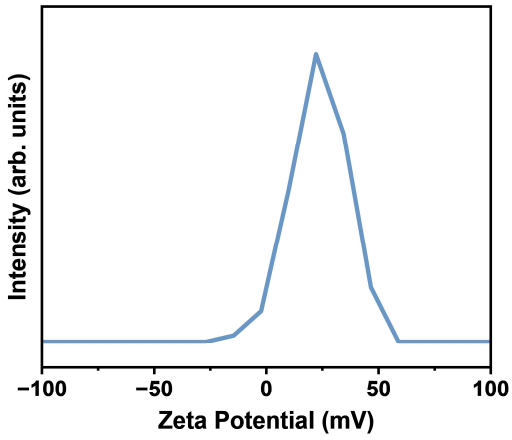

Supplementary Figure 5 | Zeta potential curve of amino mica. The results illustrate the remarkable surface positive potential (22.2 mV), owing to the existence of the amino group on the surface of amino mica.

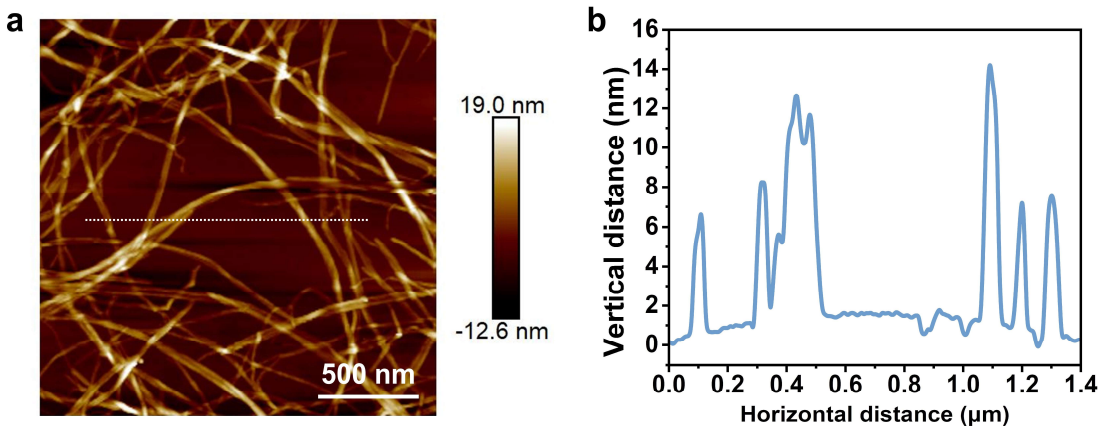

Supplementary Figure 6 | Morphological characterization of cCNF. a, AFM image of cCNF. **b**, The relative height corresponding to the line in Supplementary Figure 6a.

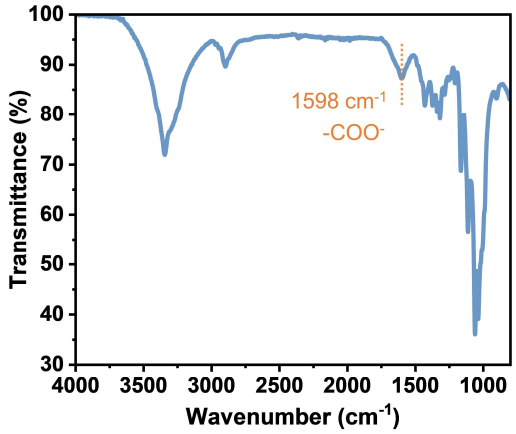

Supplementary Figure 7 | FT-IR spectrum of cCNF. The carboxyl signal peak (1598 cm^{-1}) can be observed obviously.

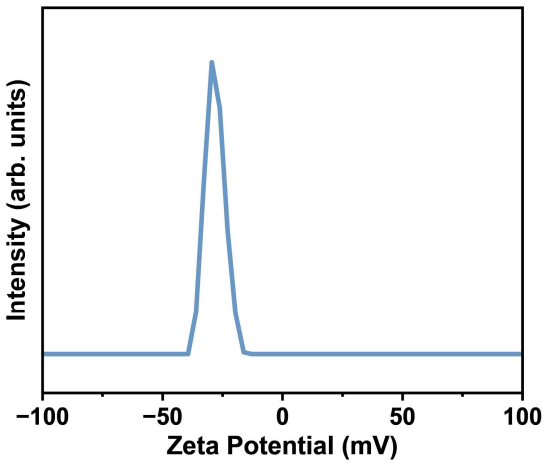

Supplementary Figure 8 | Zeta potential curve of cCNF. The results illustrate the remarkable surface negative potential (-29.4 mV), owing to the carboxyl group on the surface of cCNF.

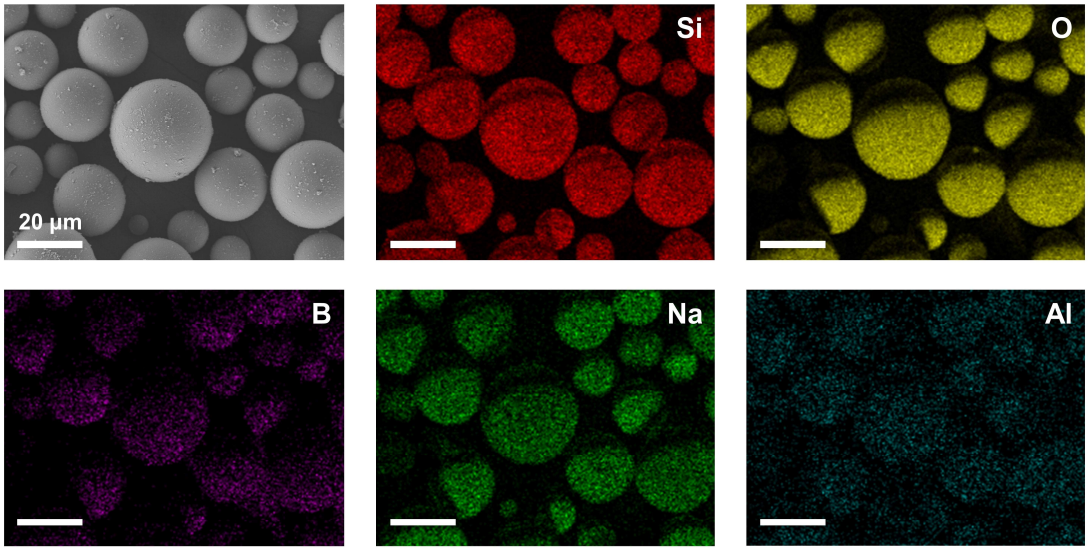

Supplementary Figure 9 | Energy-dispersive X-ray spectroscopy (EDS) mapping images of elements Si, O, B, Na, and Al for GB. The result indicates the existence of boracic sites on the surface of GB.

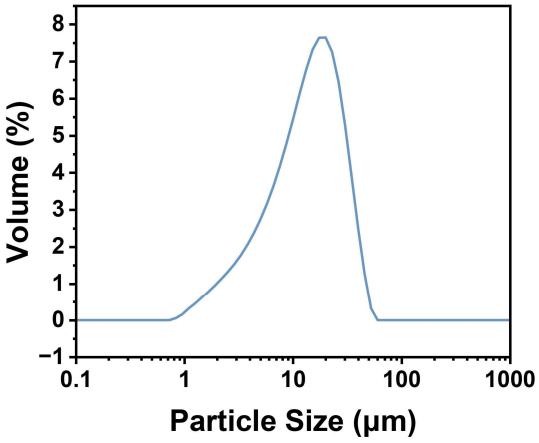

Supplementary Figure 10 | Particle size distribution of GB.

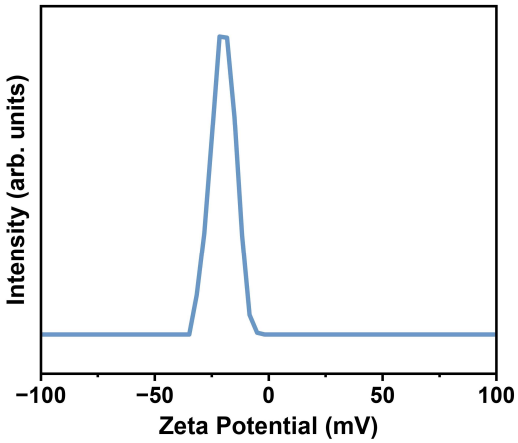

Supplementary Figure 11 | Zeta potential of GB. The results illustrate the remarkable surface negative potential (-21.5 mV) of GB.

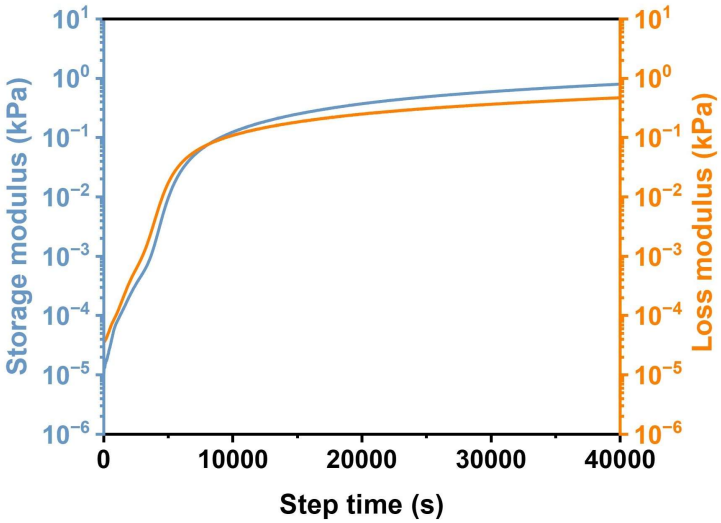

Supplementary Figure 12 | Rheological properties of the GB/PVA sample. Compared to those of the GB/PVA/qCNF sample, an assembly system of rigid cavity layers, although the storage modulus and loss modulus of the GB/PVA sample are lower, the rheological behavior of this sample is highly similar to that of the GB/PVA/qCNF sample. This further demonstrates that the major rheological properties and internal interactions of the rigid cavity layer assembly system are derived from the observable interactions between the GB and PVA.

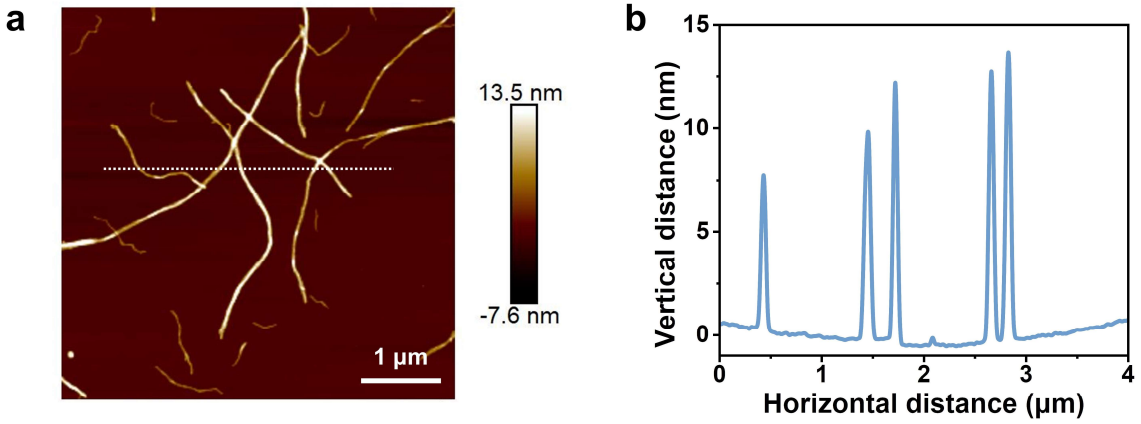

Supplementary Figure 13 | Morphological characterization of qCNF. a, AFM image of qCNF. **b**, The relative height corresponding to the line in Supplementary Figure 13a.

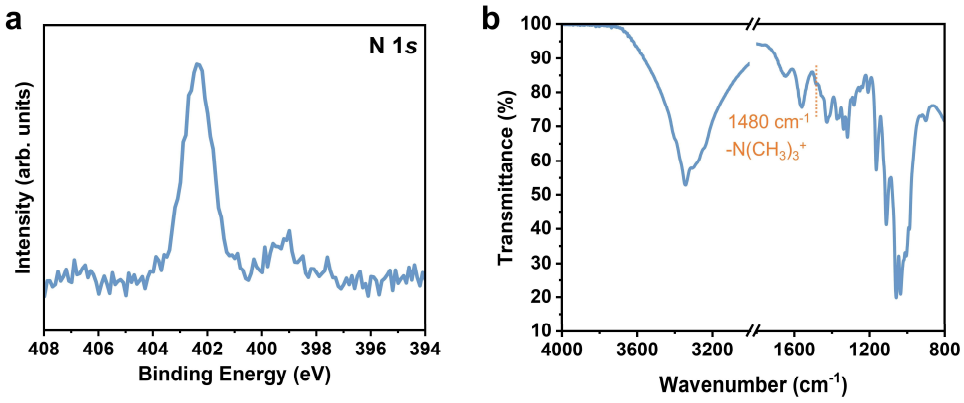

Supplementary Figure 14 | N 1*s* XPS and FT-IR spectra of qCNF. a, N 1*s* XPS spectrum of qCNF. A quaternary ammonium group signal peak can be observed in the XPS spectrum for N 1*s*. **b**, A quaternary ammonium group signal peak can be observed in the FT-IR spectrum (1480 cm^{-1}).

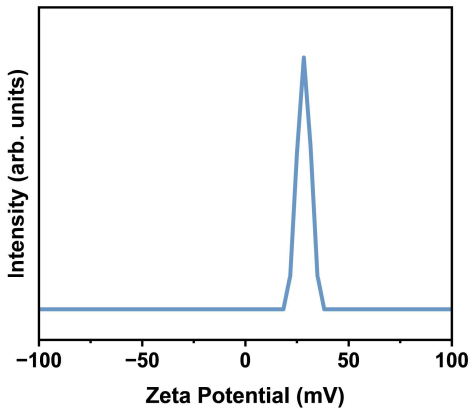

Supplementary Figure 15 | Zeta potential curve of qCNF. The results illustrate the remarkable surface positive potential (28.4 mV) of qCNF, owing to the presence of ammonium groups on the surface of the qCNF.

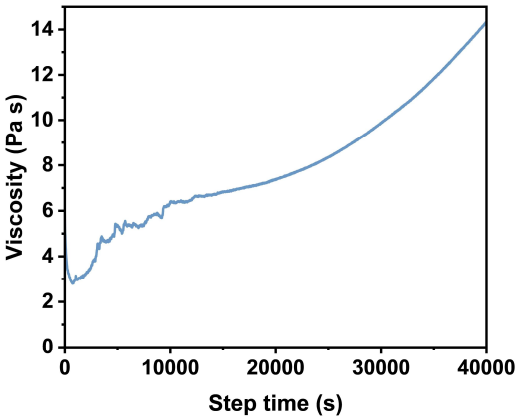

Supplementary Figure 16 | The rheological properties of the GB/PVA/qCNF initial gel of rigid cavity layer, which shows the change in viscosity with the step time.

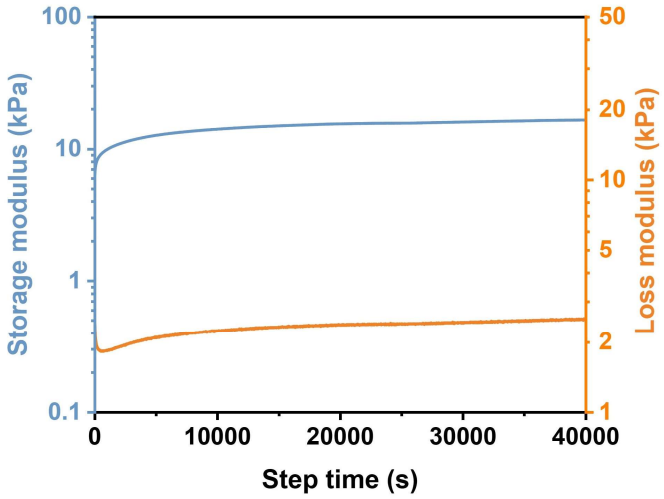

Supplementary Figure 17 | Rheological properties of the GB/qCNF sample. Compared to that of the GB/PVA/qCNF sample, an assembly system of rigid cavity layers, the rheological behavior of the GB/qCNF sample is noticeably different. The curve shows the high modulus of qCNF, which could effectively enhance the whole assembly system. However, except for the faint transition stage at the beginning of the test, the overall curve remains approximately constant, proving that there are no strong interactions between the GB and qCNF.

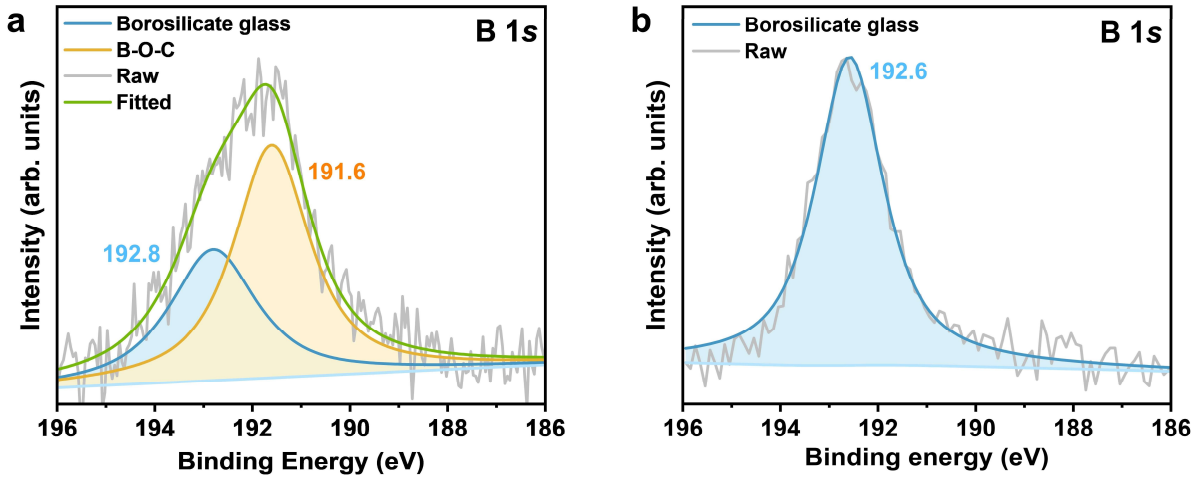

Supplementary Figure 18 | B 1*s* XPS spectra of the GB/PVA/qCNF and GB/qCNF samples. a, XPS spectrum of the GB/PVA/qCNF sample for the B 1*s* main peak fitted by two peaks at 192.8 eV (borosilicate glass matrix) and 191.6 eV (B-O-C), which are attributed to the B-O-C bond between PVA and the boracic sites on the surface of the GB. **b**, In contrast, in the B 1*s* XPS spectrum of the GB/qCNF sample, no obvious signal peak can be observed except for that of borosilicate glass (192.6 eV), which further confirms that B-O-C bonding is dominant in the fabrication of rigid cavity layers.

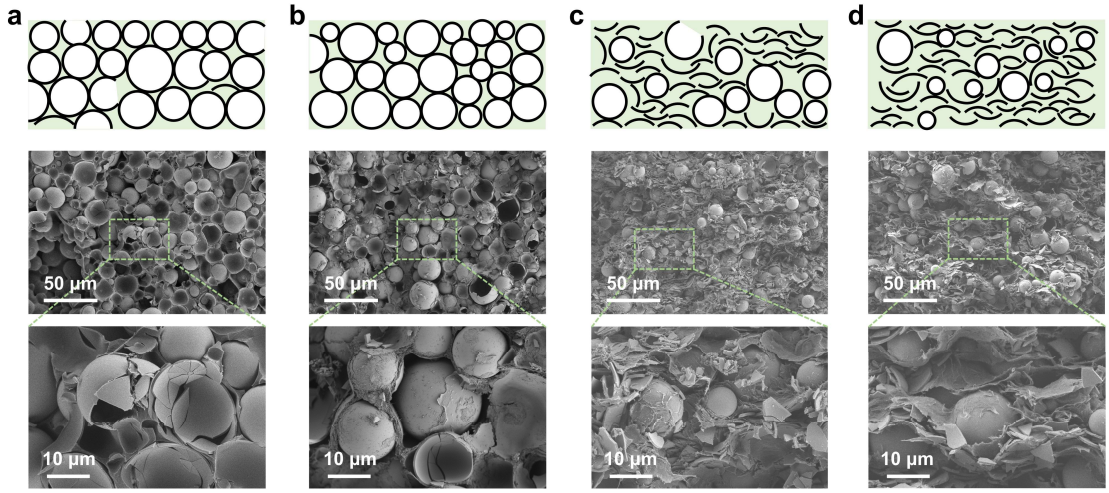

Supplementary Figure 19 | SEM images and corresponding schematic of the GB composites with various mass-to-mass ratios of PVA/qCNF. In the premise of 50 wt% GB mass content ratio of each composite, the PVA/qCNF mass content ratios are (**a**) 1:0, (**b**) 3:1, (**c**) 1:1, and (**d**) 0:1, respectively.

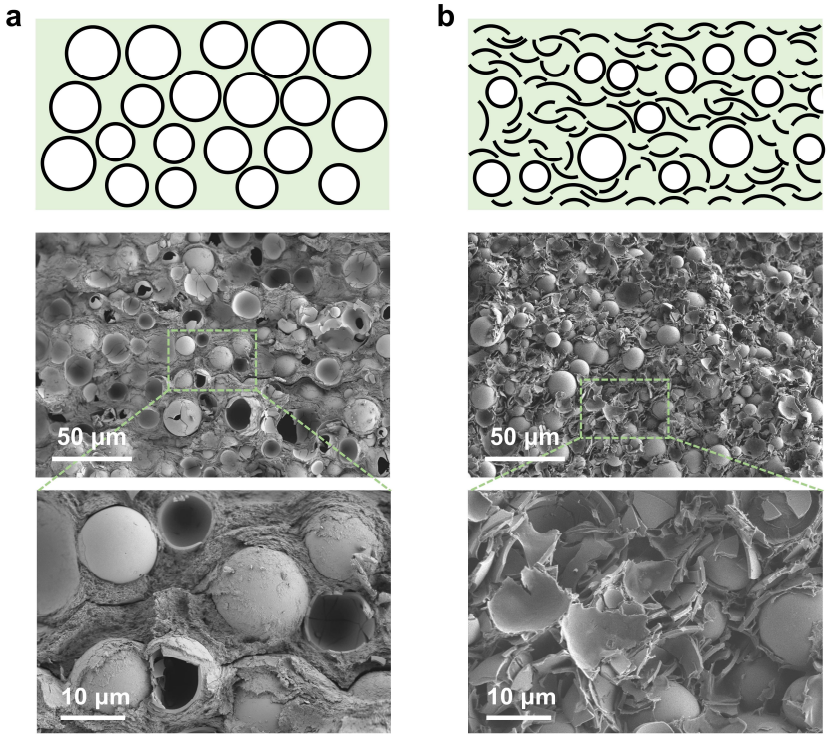

Supplementary Figure 20 | SEM images and corresponding schematic of GB composites with various mass-to-mass ratios of GB. With the premise of obtaining a 3:1 PVA/qCNF mass content ratio for each GB composite, the GB mass content ratios are (**a**) 25 wt% and (**b**) 75 wt%.

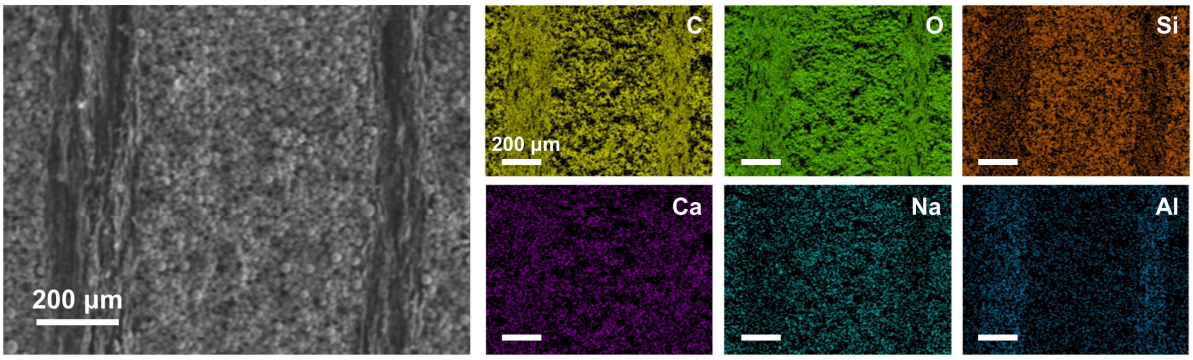

Supplementary Figure 21 | EDS mapping images of elements C, O, Si, Ca, Na, and Al for RCWSM.

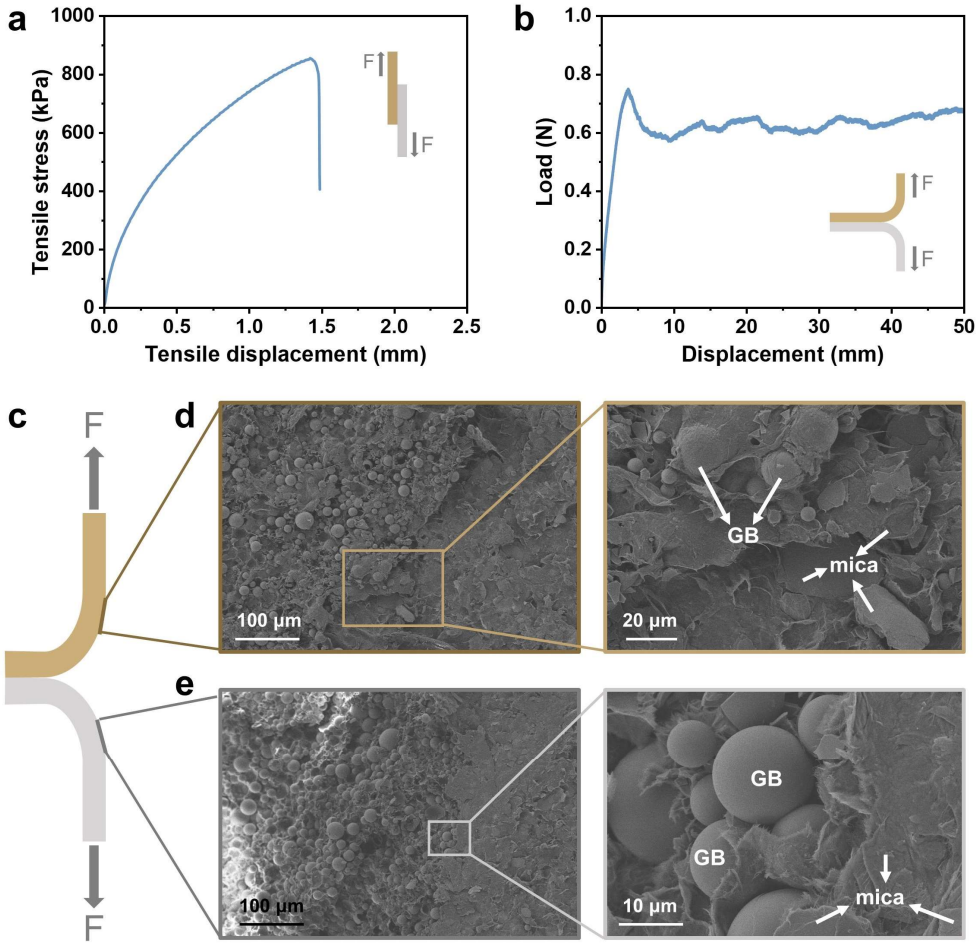

Supplementary Figure 22 | The interfacial mechanical properties of two different initial hydrogel layers. a, Tensile stress-displacement curve for the lap-shear test. **b**, Load-displacement curve for the 180° peel test. **c**, Schematic of the 180° peel test. **d**, SEM images of the rigid wall initial hydrogel layer surface after 180° peel test. **e**, SEM images of the rigid cavity layer initial hydrogel layer surface after 180° peel test. All the SEM images were obtained from the initial hydrogel after 180° peel test and dried with supercritical CO_2.

Supplementary Figure 23 | Photograph of RCWSM. The sample size is about 60 mm × 60 mm × 4 mm.

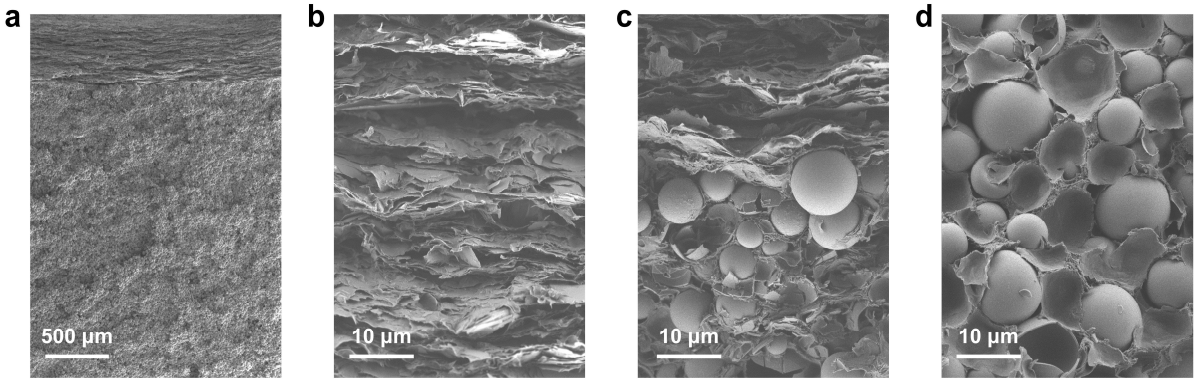

Supplementary Figure 24 | SEM images of sandwich structural material (SSM). a, Large-scale SEM image of SSM. **b**, The brick-and-mortar structure in SSM. **c**, The interface between the brick-and-mortar structure and the close-packed rigid micro hollow structure. **d**, The close-packed rigid micro hollow structure in SSM.

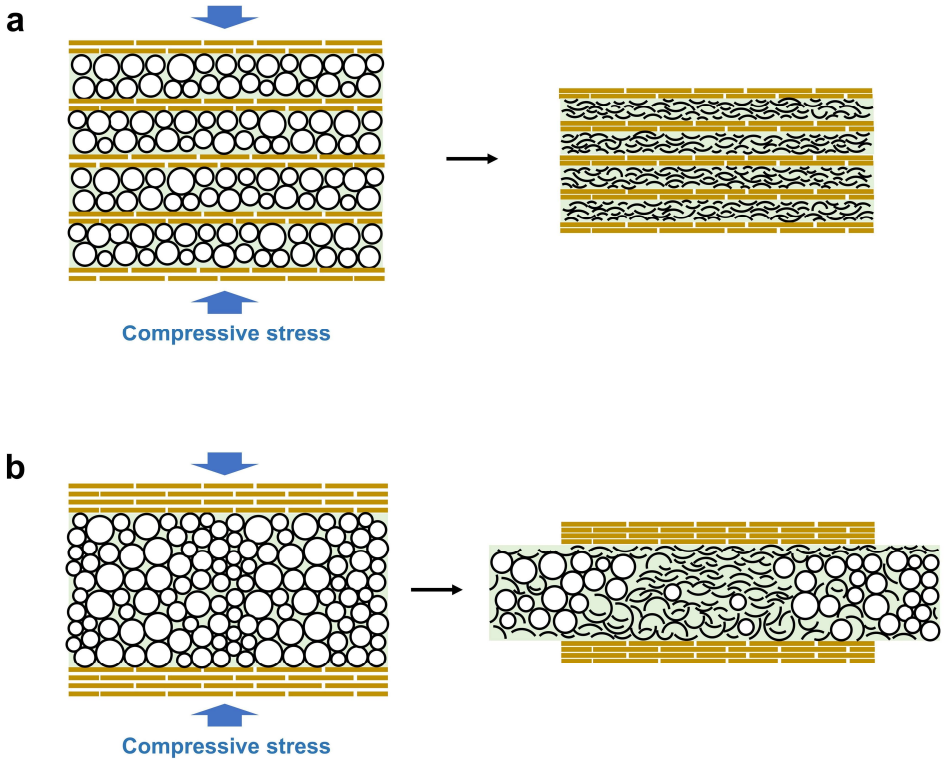

Supplementary Figure 25 | Schematic of the failure mechanism of rigid cavity-wall structure design and sandwich structure design. a, Under compressive stress, the cuttlebone-inspired rigid cavity-wall structure can effectively disperse stress concentrations to enhance the crushing failure of rigid microcavities, which can adequately absorb energy. **b**, In contrast, in the sandwich structure design, rigid microcavities will not only crush but also slide out, which is not conducive to sufficient energy absorption via crush failure. This further highlights the superiority of rigid cavity-wall structure design.

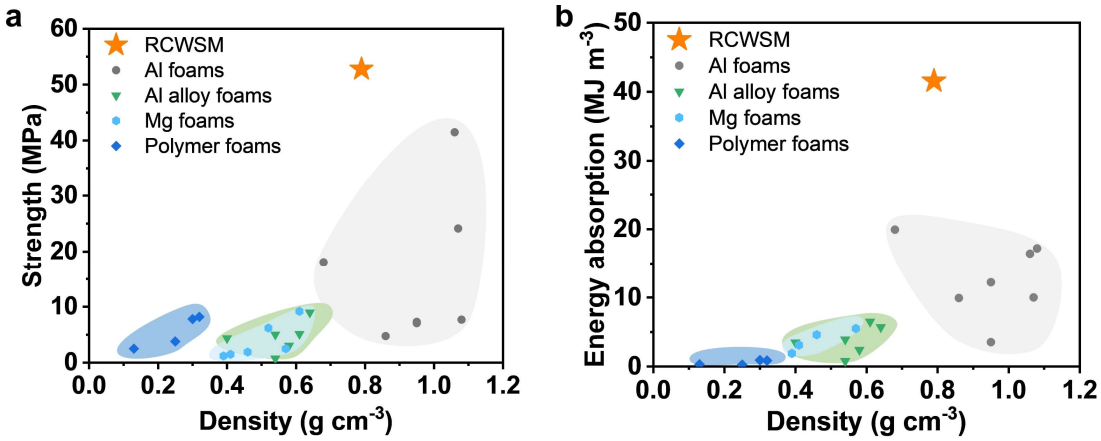

Supplementary Figure 26 | Ashby diagrams for the RCWSM and typical energy absorption materials. a, Ashby diagram of the compressive strength versus density. **b**, Ashby diagram of energy absorption versus density.

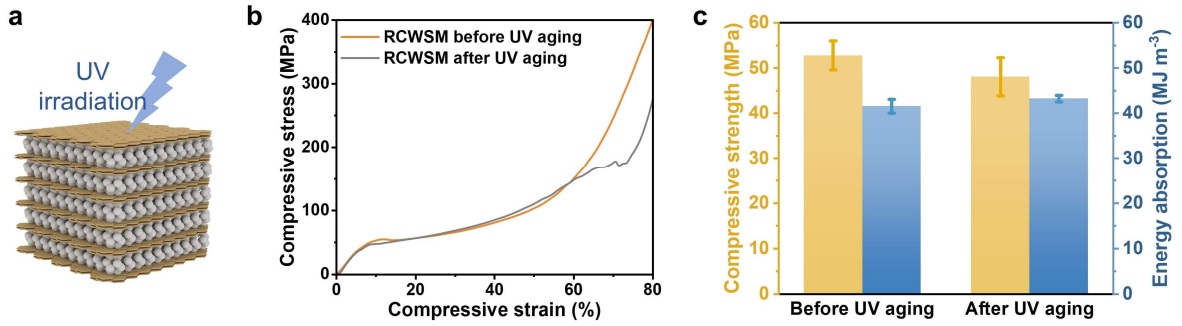

Supplementary Figure 27 | Performance of RCWSM after 20 days of UV aging treatment. **a**, Schematic of the UV aging treatment. **b**, Compressive stress-strain curve of the RCWSM before and after UV aging treatment. **c**, Compressive strength and energy absorption of the RCWSM before and after UV aging treatment. Error bars show standard deviation with 4 repeats.

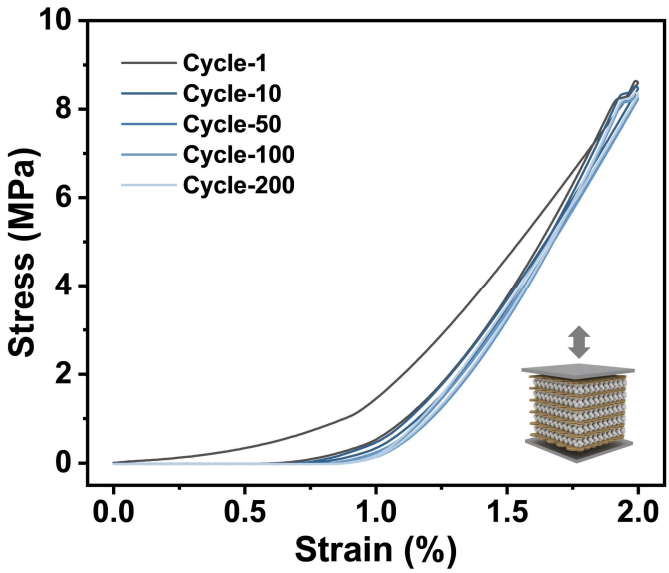

Supplementary Figure 28 | Cyclic compressive stress-strain curves of the RCWSM. Inset: schematic of the cyclic compression test for RCWSM, marked the compressive stress direction of the test.

Supplementary Table 1 | Densities of GB composites with various content ratios.

Mass content ratio (GB/PVA/qCNF)	Density (g cm^{-3})
4:9:3	0.88
4:3:1	0.58
12:3:1	0.80
2:2:0	0.62
2:1:1	0.84
2:0:2	0.87

Supplementary Table 2 | Comparison of the compressive strength and specific compressive strength of cuttlebone-inspired RCWSM and typical energy absorption materials.

Samples	Density ($g\ cm^{-3}$)	Compressive strength (MPa)	Specific compressive strength [$MPa/(Mg\ m^{-3})$]	References
Al foams	1.06	41.47	39.25	Ref. 1
	1.07	24.14	22.56	
	0.68	18.10	26.58	Ref. 2
	0.86	4.75	5.50	Ref. 3
	0.95	7.31	7.74	
	1.08	7.70	7.13	
	0.95	7.07	7.48	Ref. 4
Al-Ti alloy foams	0.54	0.74	1.37	Ref. 5
	0.58	3.06	5.28	
	0.61	5.13	8.41	
	0.64	8.96	14.00	
Mn-Al alloy foams	0.54	5.03	9.33	Ref. 6
Al-Si alloy foams	0.40	4.36	10.88	Ref. 7
PVC foams	0.13	2.50	19.23	Ref. 8
	0.30	7.80	26.00	
PU foams	0.32	8.20	25.63	Ref. 8
	0.25	3.80	15.45	
Mg foams	0.57	2.50	4.37	Ref. 9
	0.46	1.90	4.10	
	0.41	1.50	3.62	
	0.39	1.20	3.12	
	0.61	9.18	15.05	Ref. 10
	0.52	6.20	11.92	
RCWSM	**0.79**	**52.77**	**66.79**	**This work**

Supplementary Table 3 | Comparison of energy absorption and specific energy absorption for cuttlebone-inspired RCWSM and typical energy absorption materials.

Samples	Density ($g\ cm^{-3}$)	Energy absorption ($MJ\ m^{-3}$)	Specific energy absorption ($J\ g^{-1}$)	References
Al foams	1.06	16.44	15.56	Ref. 1
	1.07	10.01	9.36	
	0.68	19.93	29.27	Ref. 2
	0.86	9.92	11.48	Ref. 3
	0.95	12.22	12.93	
	1.08	17.21	15.94	
	0.95	3.53	3.74	Ref. 4
Al-Ti alloy foams	0.54	0.79	1.46	Ref. 5
	0.58	2.40	4.14	
	0.61	6.50	10.66	
	0.64	5.71	8.92	
Mn-Al alloy foams	0.54	3.92	7.27	Ref. 6
Al-Si alloy foams	0.40	3.47	8.66	Ref. 7
PVC foams	0.13	0.31	2.36	Ref. 8
	0.30	0.92	3.07	
PU foams	0.32	0.87	2.72	Ref. 8
	0.25	0.26	1.04	
Mg foams	0.57	5.50	9.61	Ref. 9
	0.46	4.60	9.93	
	0.41	3.10	7.48	
	0.39	1.90	4.93	
RCWSM	**0.79**	**41.55**	**52.60**	**This work**

References

1. Li, C., Li, C. & Wang, Y. Compressive behavior and energy absorption capacity of unconstrained and constrained open-cell aluminum foams. *Adv. Compos. Lett.* **29**, 1-4 (2020).

2. Novak, N.*, et al.* Compressive behaviour of closed-cell aluminium foam at different strain rates. *Materials* **12,** 4108 (2019).

3. Soni, B. & Biswas, S. Effects of cell parameters at low strain rates on the mechanical properties of metallic foams of Al and 7075-T6 alloy processed by pressurized infiltration casting method. *J. Mater. Res.* **33**, 3418-3429 (2018).

4. Hassani, A., Habibolahzadeh, A. & Bafti, H. Production of graded aluminum foams via powder space holder technique. *Mater. Des.* **40**, 510-515 (2012).

5. Zhang, W., Zheng, X., Zhu, C. & Long, W. Effect of Ti content on the cell structure and compressive and energy absorption properties of Al_3Ti/Al6061 foam composite. *J. Alloy. Compd.* **957**, 170321 (2023).

6. Xia, X., Feng, H., Zhang, X. & Zhao, W. The compressive properties of closed-cell aluminum foams with different Mn additions. *Mater. Des.* **51**, 797-802 (2013).

7. Yang, X., Xie, M., Li, W., Sha, J. & Zhao, N. Controllable design of structural and mechanical behaviors of Al–Si foams by powder metallurgy foaming. *Adv. Eng. Mater.* **24**, 2200125 (2022).

8. Saha, M. C.*, et al.* Effect of density, microstructure, and strain rate on compression behavior of polymeric foams. *Mater. Sci. Eng. A* **406**, 328-336 (2005).

9. Osorio-Hernández, J. O.*, et al.* Manufacturing of open-cell Mg foams by replication process and mechanical properties. *Mater. Des.* **64**, 136-141 (2014).

10. Lu, G. Q., Hao, H., Wang, F. Y. & Zhang, X. G. Preparation of closed-cell Mg foams using SiO_2-coated $CaCO_3$ as blowing agent in atmosphere. *Trans. Nonferrous Met. Soc. China* **23**, 1832-1837 (2013).